A three-dimensional synthesis inversion of the molecular hydrogen cycle: Sources and sinks budget and implications for the soil uptake

Philippe Bousquet, C. Yver, I. Pison, Y. Li, A. Fortems, D. Hauglustaine, S. Szopa, P. Rayner, P. Novelli, R. Langenfelds, et al.

A three-dimensional synthesis inversion of the molecular hydrogen cycle: Sources and sinks budget and implications for the soil uptake

P. Bousquet,[1,2] C. Yver,[1] I. Pison,[1,2] Y. S. Li,[1] A. Fortems,[1] D. Hauglustaine,[1] S. Szopa,[1] P. J. Rayner,[1,3] P. Novelli,[4] R. Langenfelds,[5] P. Steele,[5] M. Ramonet,[1] M. Schmidt,[1] P. Foster,[6] C. Morfopoulos,[7] and P. Ciais[1]

Received 8 June 2010; revised 13 September 2010; accepted 21 September 2010; published 11 January 2011.

[1] Our understanding of the global budget of atmospheric hydrogen (H_2) contains large uncertainties. An atmospheric Bayesian inversion of H_2 sources and sinks is presented for the period 1991–2004, based on a two networks of flask measurement stations. The types of fluxes and the spatial scales potentially resolvable by the inversion are first estimated from an analysis of the correlations of errors between the different processes and regions emitting or absorbing H_2. Then, the estimated budget of H_2 and its uncertainties is presented and discussed, for five groups of fluxes and three groups of large regions, in terms of mean fluxes, seasonal and interannual variations, and long-term trends. One main focus of the study is the improvement of the estimate of H_2 soil uptake, which is the largest sink of H_2. Various sensitivity tests are performed defining an ensemble of more than 20 inversions. We show that inferring a robust estimate of the H_2 soil uptake requires to prescribe the prior magnitude of some other sources and sinks with a small uncertainty. Doing so an estimate of the H_2 soil uptake of -62 ± 3 Tg y^{-1} is inferred for the period 1991–2004 (the uncertainty is the residual error after inversion). The inferred soil H_2 sink presents a negative long-term trend that is qualitatively consistent with a bottom-up process-based model.

Citation: Bousquet, P., et al. (2011), A three-dimensional synthesis inversion of the molecular hydrogen cycle: Sources and sinks budget and implications for the soil uptake, *J. Geophys. Res.*, *116*, D01302, doi:10.1029/2010JD014599.

1. Introduction

[2] Molecular hydrogen (H_2) is a product of the oxidation chain of methane (CH_4), carbon monoxide (CO) and volatile organic compounds (VOCs). With a lifetime of around 2–3 years [*Conrad and Seiler*, 1980; *Novelli et al.*, 1999; *Price et al.*, 2007; *Xiao et al.*, 2007], H_2 is transported by atmospheric circulation from one hemisphere to the other, being intermediate between short-lived gases with regional and local influences such as carbon monoxide (CO) and formaldehyde (HCHO), and long-lived gases with global influence such as methane (CH_4) or carbon dioxide (CO_2). The present global mean mixing ratio of H_2 is about 530 ppb [*Novelli et al.*, 1999], making it the second reduced atmospheric trace gas after methane (~1800 ppb). H_2 is indirectly controlling the budget of CH_4, CO, and volatile organic compounds (VOCs) via its concurrent oxidation by OH radicals and its production from HCHO. H_2 has also received recent interest as a possible alternative to fossil fuel in surface transportation through the use of H_2-based fuel cells in cars. Such cars would improve air quality by not emitting ozone precursors such as nitrogen oxides (NOx) or VOCs. However, the leakage of H_2 may reduce the hydroxyl radical (OH) concentrations and then contribute an increase of the atmospheric abundance of CH_4, and a modification the oxidation capacity of the troposphere [*Warwick et al.*, 2004]. As CH_4 is a major greenhouse gas, present and future changes of H_2 abundance in the atmosphere are important to understand and monitor in the context of a changing climate.

[3] The regular monitoring of H_2 mole fractions in the atmosphere started in 1989 and has since developed into a network of more than 80 stations worldwide [*Novelli et al.*, 1999; *Francey et al.*, 1998; *Langenfelds et al.*, 2002; *Yver et al.*, 2009] (http://www.iau.uni-frankfurt.de/eurohydros/). Most data are from weekly or biweekly flask sampling while continuous monitoring is conducted at only a small number of sites. As for all trace gases, the surface measurement network of H_2 is not evenly spread around the globe,

[1]Laboratoire des Sciences du Climat et de l'Environnement, Gif sur Yvette, France.
[2]Université de Versailles Saint Quentin en Yvelines, Versailles, France.
[3]Now at School of Earth Sciences, University of Melbourne, Parkville, Victoria, Australia.
[4]Earth System Research Laboratory, NOAA, Boulder, Colorado, USA.
[5]Centre for Australian Weather and Climate Research, CSIRO Marine and Atmospheric Research, Aspendale, Victoria, Australia.
[6]Department of Earth Sciences, University of Bristol, Bristol, UK.
[7]Division of Biology, Imperial College of London, London, UK.

0148-0227/11/2010JD014599

with large unresolved areas such as tropical continents and Siberia, and concentrations of stations in developed areas such as North America or Europe.

[4] H_2 is emitted by anthropogenic activities such as traffic and industry, by biofuel and biomass burning, and during terrestrial and oceanic fixation of N_2. These surface emissions represent about half of the global H_2 source, the other half being the chemical production of H_2 in the atmosphere by oxidation of CH_4 and VOCs, An important intermediate compound of these tropospheric oxidation chains is formaldehyde (HCHO) which is rapidly photolysed (lifetime~1 day) in CO and H_2, through two possible chemical paths [*Warneck*, 1988]. HCHO formation is due to tropospheric oxidation of CH_4, with an important contribution of VOCs oxidation above continents [*Price et al.*, 2007]. *Ehhalt and Rohrer* [2009] provide the most recent and complete review of the H_2 budget. Gridded surface emissions for H_2 surface sources are available for fires [*van der Werf et al.*, 2006] and usually scaled from CO emissions using classical inventories [*Olivier and Berdowski*, 2001] because no inventory is available for other sources of H_2. Photochemical production is often estimated using atmospheric chemistry-transport models [*Hauglustaine et al.*, 2004]. H_2 emissions linked to N_2 fixation can be scaled from other trace gas emission maps, such as CO for marine emissions and NOx for terrestrial emissions [*Hauglustaine and Ehhalt*, 2002].

[5] Unlike many tropospheric reactive gases, the main sink of H_2 is not its oxidation by the OH radical (20–40%) but its deposition at the surface (60–80%). The H_2 soil uptake is largely uncertain because the underlying mechanisms are not yet completely understood. They involve removal by bacteria in soils [*Yonemura et al.*, 2000b] and by enzymatic activity of soil hydrogenases [*Conrad and Seiler*, 1981]. Many parameters seem to play a role in the H_2 uptake by soils. Higher temperature, lower compaction, and higher carbon content due to dead plant material are factors that lead to increasing H_2 deposition velocity [*Yonemura et al.*, 1999, 2000a; *Yonemura et al.*, 2000b]. Soil moisture was found to be a key parameter [*Conrad and Seiler*, 1981; *Yonemura et al.*, 1999, 2000a, 2000b] controlling the rate of H_2 uptake by soils, with a value of ~20% saturation corresponding to maximum uptake, smaller saturations leading to reduced microbial activity and higher saturations further inhibiting H_2 diffusion in the soil column [*Smith-Downey et al.*, 2006]. Owing to its complex biology, H_2 soil uptake is modeled under more or less simplified assumptions. For example, *Hauglustaine and Ehhalt* [2002] used the net primary productivity (NPP) to constrain the distribution of the dry deposition velocity for CO [*Muller*, 1992; *Müller and Brasseur*, 1995; *Brasseur et al.*, 1998] and applied a constant ratio of $vd_{H2}/vd_{CO} = 1.5$ based on studies by *Yonemura et al.* [2000a, 2000b] and *Hough* [1991]. In their study, *Price et al.* [2007] uses a uniform deposition velocity over non-snow-covered land with surface temperatures above 0°C. Overall, uncertainties in the magnitude and the location of H_2 sources and sinks remain large, as shown by the complete synthesis produced by *Ehhalt and Rohrer* [2009, Table 1].

[6] Atmospheric inversions combine H_2 atmospheric observations, a chemistry-transport model, and prior information on both surface fluxes, and sources and sinks within the atmosphere, in order to estimate H_2 sources and sinks and their uncertainties. Atmospheric inversions have already been successfully developed to study the budget of inert gases such as CO_2 [*Rayner et al.*, 1999; *Bousquet et al.*, 2000; *Gurney et al.*, 2002; *Baker et al.*, 2006], long-lived gases such as CH_4 [*Bergamaschi et al.*, 2005; *Bergamaschi et al.*, 2009; *Bousquet et al.*, 2006; *Chen and Prinn*, 2006], reactive gases such as CO [*Pétron et al.*, 2004; *Chevallier et al.*, 2009; *Fortems-Cheiney et al.*, 2009] and methyl chloroform [*Prinn et al.*, 2005; *Krol and Lelieveld*, 2003; *Bousquet et al.*, 2005]. Several studies have produced forward modeling of H_2 concentrations in the atmosphere [*Hauglustaine and Ehhalt*, 2002; *Schultz et al.*, 2003] and of the deuterium content [*Rahn et al.*, 2003; *Price et al.*, 2007; *Ehhalt and Rohrer*, 2009]. These forward modeling studies have provided the first constraints of H_2 sources and sinks, in light of the mismatches between modeled and observed H_2 concentrations. *Xiao et al.* [2007] have used a 2-D latitude-vertical 12-box model for atmospheric chemistry in an inversion framework to estimate the magnitude and variability of H_2 sources and sinks for four semihemispheres over the 1993–2004 period. Following *Chevallier et al.* [2005], *Pison et al.* [2009] recently developed a multispecies inversion of CH_4, CO, and H_2 sources and sinks, based on variational assimilation. Their approach has the advantage to estimate surface emission at model resolution, avoiding aggregation errors [*Kaminski et al.*, 2001], but does not allow performing a lot of sensitivity tests because of its computational cost.

[7] This paper provides an analysis of the H_2 budget over the 1991–2004 period, using a Bayesian atmospheric inversion model and a 3-D chemistry transport model forced by observed winds. The objective is to estimate the magnitude of the various terms of the H_2 budget, for large regions and globally, by inversion of atmospheric observations, with a focus on the magnitude, the variability and the uncertainties associated with the soil uptake.

[8] After presenting the method (section 2), the processes and regions discussed in the paper are chosen according to an analysis of the structure of error of the H_2 fluxes for seven scenarios, gradually increasing the constraint on soil uptake (section 3). Section 4 is devoted to the H_2 budget for the 1991–2004 period, both on a process-based and on a region-based point of view. Then, the variability of H_2 fluxes is presented and discussed for seasonal, year-to-year, and long-term variations (section 5). Finally, the impact of the seven scenarios on the magnitude and robustness of the soil uptake estimate is discussed (section 6).

2. Inversion Settings

2.1. General Inverse Framework

[9] The inverse model used in this study is described in detail in the work of *Bousquet et al.* [2005] for methyl-chloroform inversion and in the work of *Bousquet et al.* [2006] for methane inversion. Briefly, H_2 emissions from different regions of the globe and from distinct processes (biomass and biofuel burning, fossil fuel use, N_2 fixation by land and ocean organisms, photochemical production) and loss through soil uptake and OH oxidation are inferred within their respective uncertainties, by matching modeled H_2 concentrations with observations, within their uncertainties, in a Bayesian formalism [*Bousquet et al.*, 2006].

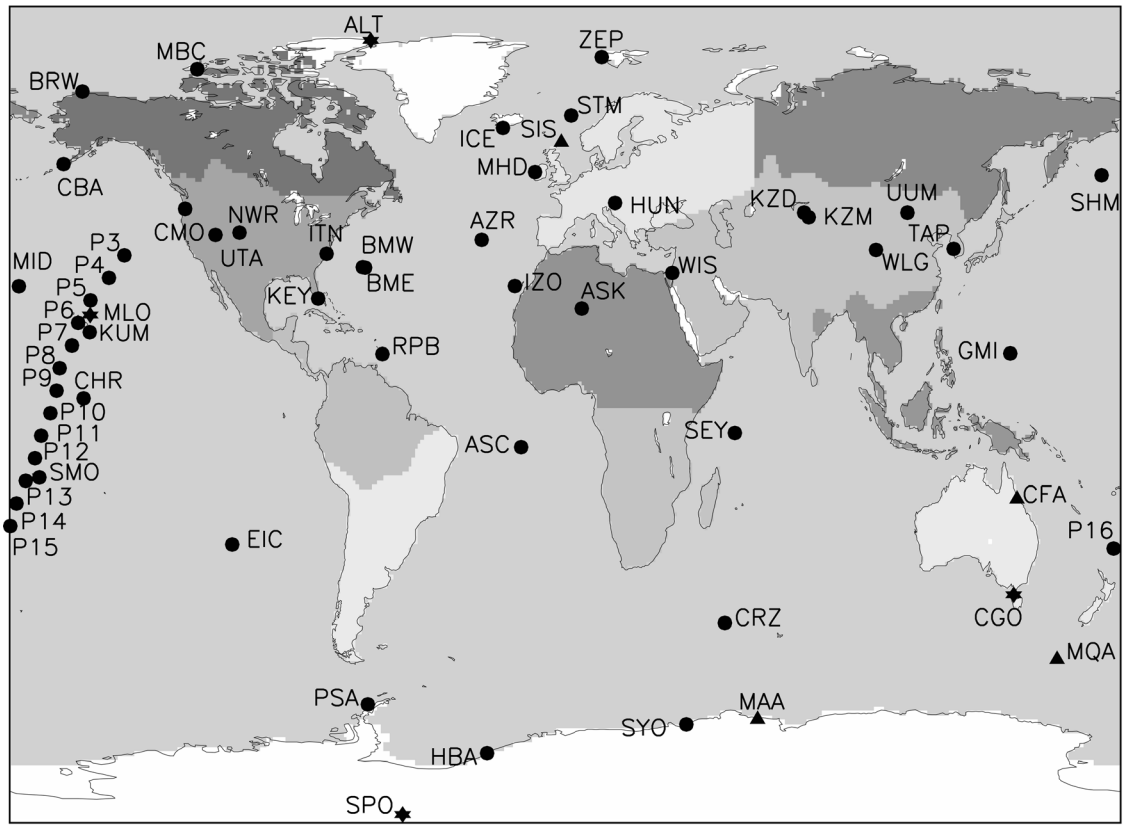

Figure 1. Map of the 12 regions (11 land regions and 1 ocean region) and of the 62 atmospheric stations used in the inversion. Different symbols represent different networks: circles for NOAA, triangles for CSIRO, and stars when both NOAA and CSIRO operate (ALT, CGO, MLO, and SPO).

Such an inversion system requires: global observations of H_2 mixing ratios, responses to different sources and sinks at the location and time of the observations, and prior information on the magnitude and spatiotemporal distribution of sources and sinks.

2.2. Atmospheric Observations

[10] Weekly flask observations at up to 62 sampling sites from NOAA network with 54 sites [*Novelli et al.*, 1999] and CSIRO network for eight sites [*Steele et al.*, 1992] are averaged to monthly means and used in the inversion (Figure 1). Prior uncertainties on observations are prescribed according to a scaling of CH_4 uncertainties, given by the GLOBALVIEW-CH_4 global data product when available [*GLOBALVIEW-CH$_4$*, 2005], or else by the standard deviation of individual flask data within each month with a minimum monthly error of 5 ppb (1 sigma). The scaling factor is determined as the ratio between the global H_2 mixing ratio and the global CH_4 mixing ratio for the year 2000. We are lacking information to define observational uncertainties for H_2, which should represent model-observation mismatches, and therefore should include both model and measurement errors [*Tarantola*, 1987]. Our approach allows keeping the relative weight between stations as in the analysis of uncertainties performed in GLOBALVIEW-CH4. No correlations of errors are used between monthly H_2 observations. Two sensitivity tests, increasing and decreasing observation errors globally, are performed to estimate the impact of the observation errors on the inverted fluxes. Observation uncertainties range between ±5 and ±40 ppb depending on the sampling site, with a median of ±9 ppb (1-sigma). In comparison, the maximum seasonal peak to peak amplitude at Alert (Canada) is 80 ppb, and the interhemispheric H_2 annual gradient is larger than 50 ppb (Figure 2). The north-south annual gradient also reveals smaller H_2 mixing ratios in the Northern Hemisphere as compared to the Southern Hemisphere because of the importance of the soil uptake in the Northern Hemisphere (Figure 2). Observations after 2004 could not be used because of an unresolved drift in the NOAA/ESRL observations. Because the NOAA/ESRL network is the main source of observations of this work, we decided to limit the period of inversion to 1991–2004.

[11] NOAA and CSIRO observations are reported on different scales. Therefore possible offsets have to be accounted for. We have calculated the NOAA-CSIRO difference from the deseasonalized monthly time series (subtraction of a mean seasonal cycle based on *Thoning et al.* [1989]) at stations where both NOAA and CSIRO perform measurements (ALT, MLO, CGO, SPO, Figure 1). The mean difference for these four sites is then fitted with two lines, corresponding to two distinct periods: the first one shows a decreasing difference (from 1991 to 1998) and the second one shows an increasing difference (from 1998 to 2004). We include different sensitivity tests in section 4.3 to estimate the impact of these network offsets on the inferred

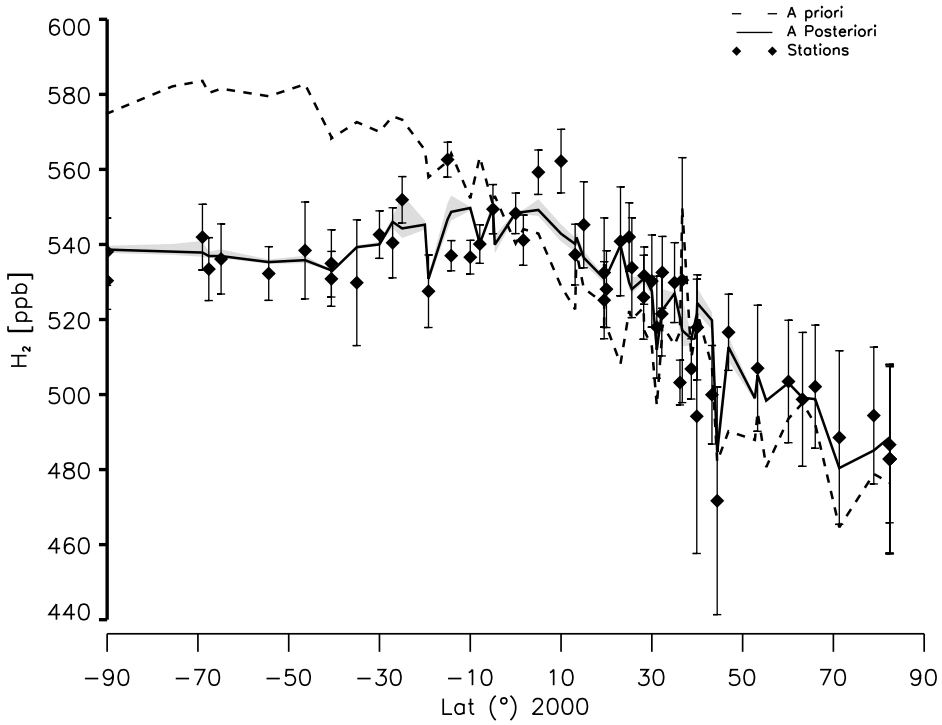

Figure 2. Annual north-to-south gradient of H2 in the atmosphere (in ppb). Symbols represent annual mean observations at stations for the year 2000 (black diamonds). Error bars are the uncertainty used in the inversion (1-sigma). Solid line represents the fit obtained after inversion for the reference scenario (S_{ref}). The dotted line represents the fit obtained before inversion, with the unbalanced prior fluxes. The gray area represents the range of the ensemble of inversions performed.

fluxes. Observations are gathered in a vector $\mathbf{y}^0$ associated with the diagonal variance-covariance matrix for observational uncertainties **R**.

2.3. Atmospheric Chemistry-Transport Model

[12] The responses of atmospheric H_2 to the flux of the different sources and sinks are simulated on a monthly basis by the three-dimensional chemistry-transport model LMDZ-INCA [*Hauglustaine et al.*, 2004]. Response functions for surface pulse emissions of one month are calculated for the period 1991–2004 with the offline version of LMDZ-INCA for atmospheric transport with retrotransport capabilities [*Hourdin and Talagrand*, 2006] forced by ECMWF-ERA40 analyzed winds [*Uppala et al.*, 2005]. The retrotransport allows saving some computing time by performing one simulation per station each month (total of 64 stations), instead of one simulation per process and per region each month (total of 7 processes × 12 regions = 84). Each 1-month pulse is build from the retroplumes, with 1 month of emission and 11 months of dispersion. Because the H_2 mixing ratios do not exhibit any significant long-term trend in the atmosphere, the response functions for the OH loss are calculated only for year 2000 and used for all the other years of the inversion period 1991–2004. The same simplification is done for photochemical production. Doing so for OH loss and photochemical production, the impact of varying meteorology affecting the chemical part of the inverse model is neglected. The modeled response functions are gathered in the Jacobian matrix **H**.

2.4. Prior Flux Information

[13] The prior distribution of surface H_2 emissions (except fires) are based on a scaling of CO emissions from the EDGAR3.2 inventory [*Olivier and Berdowski*, 2001], according to [*Hauglustaine and Ehhalt*, 2002]. H_2 emissions linked to N_2 fixation are scaled from CO emission maps for marine emissions and from NOx emission maps for terrestrial emissions [*Hauglustaine and Ehhalt*, 2002]. H_2 emissions from fires are taken from the GFED-V2 inventory [*van der Werf et al.*, 2006]. We divide the world into 11 continental regions and one oceanic region, for which we solve separately for a linear combination of different sources and sinks each month. The fluxes considered are photochemical production, emissions due to biomass and biofuel burning, fossil fuels, N_2 fixation by land and ocean ecosystems, loss due to soil uptake and OH loss. The region map (Figure 1) is derived from the region map of the TRANSCOM project (http://www.purdue.edu/transcom/). The prior distribution of soil uptake is taken according to *Hauglustaine and Ehhalt* [2002] and extracted from a simulation of the LMDZ-INCA chemistry model for year 2000 [*Hauglustaine et al.*, 2004]. The (3-D) distribution and magnitude of the prior HCHO photochemical production and OH loss within the atmosphere are extracted from the same simulation of the LMDZ-INCA chemistry model. Uncertainties on prior fluxes are originally set at ±100% of each regional flux for each month, with spatially and temporally uncorrelated errors. A minimum uncertainty of ±0.2 Tg per month per region in the photochemical production flux in the air column over each inversion region is used in

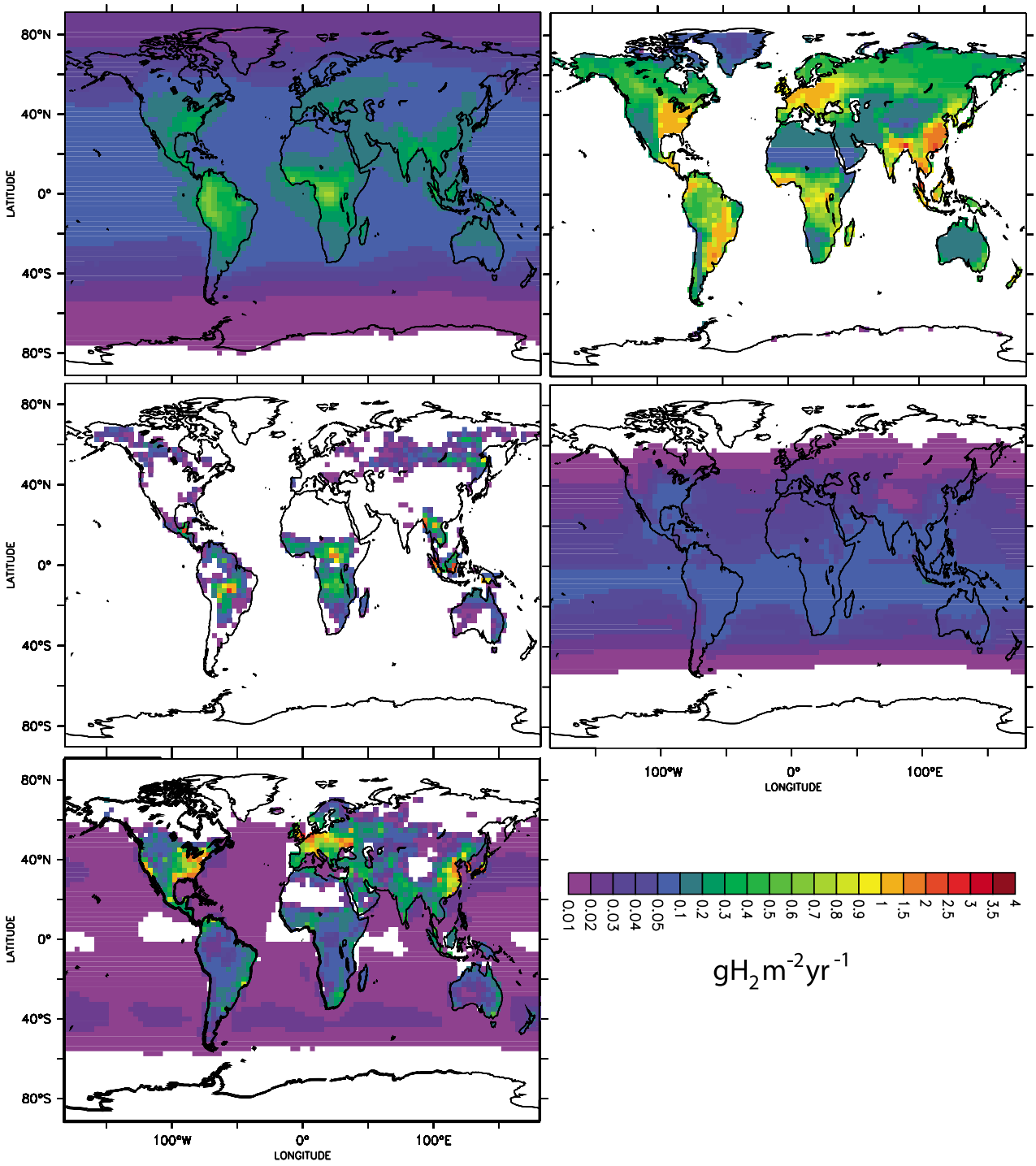

Figure 3. Prior distribution of (left) H_2 sources and (right) sinks in $gH_2.m^{-2}.yr^{-1}$ with the same nonlinear scale for all sources and sinks. Note that values below 0.01 $gH_2.m^{-2}.yr^{-1}$ are not plotted. Figure 3 (left), from top to bottom: chemical production, biomass and biofuel burning related emissions, fossil and N_2 fixation related emissions. Figure 3 (right), from top to bottom: surface uptake by soils, loss by OH oxidation. Volume sources and sinks have been summed up over altitude.

order to avoid too small prior uncertainty. These prior uncertainties are varied in the different scenarios (section 3). The prior interannually varying OH field is "preoptimized" through a preliminary inversion of methyl-chloroform atmospheric observations (see more details of this method in the work of *Bousquet et al.* [2005]). Prior OH loss is then calculated using H_2 concentrations and reaction rate for the year 2000. Doing so, only OH radicals contribute to the interannual variations of the prior OH loss. The spatial distribution of prior sources and sinks is shown in Figure 3. One can notice the importance of northern midlatitudes for fossil and N_2 related emissions, for soil uptake, and the importance of the tropics for the volume sources (photochemical production) and sinks (OH). Biomass and biofuel burning appear important within the tropics and for middle to high northern latitudes. Annual prior fluxes are gathered in the control vector $\mathbf{x}^b$ associated with the diagonal variance-covariance matrix **B**. The last element of $\mathbf{x}^b$ is the magnitude of a global offset C_0 representing the global initial concentration of H_2, as seen by the observations used, at the beginning of the inversion period.

2.5. Inversion Solving

[14] Contributions of monthly H_2 surface sources, monthly soil uptake, monthly HCHO atmospheric production, and monthly OH atmospheric loss are combined in the inversion system to optimally fit monthly averages of H_2 mixing ratios at up to 62 sampling sites (Figure 1). Minimizing the Bayesian cost function $J(\mathbf{x})$:

$$J(\mathbf{x}) = \frac{1}{2}\left(\mathbf{y}^0 - \mathbf{H}\mathbf{x}\right)^T \mathbf{R}^{-1}\left(\mathbf{y}^0 - \mathbf{H}\mathbf{x}\right) + \frac{1}{2}\left(\mathbf{x} - \mathbf{x}^b\right)^T \mathbf{B}^{-1}\left(\mathbf{x} - \mathbf{x}^b\right)$$

leads to the analytical expression $\mathbf{x}^a$ which is the magnitude of the monthly optimized H_2 sources and sinks for the 11 large regions considered [*Tarantola*, 1987]:

$$\mathbf{x}^a = \mathbf{x}^b + \left(\mathbf{H}^T\mathbf{R}^{-1}\mathbf{H} + \mathbf{B}^{-1}\right)^{-1}\mathbf{H}^T\mathbf{R}^{-1}\left(\mathbf{y}^0 - \mathbf{H}\mathbf{x}^b\right)$$

and to the uncertainties attached to $\mathbf{x}^a$ [*Tarantola*, 1987]:

$$\mathbf{A} = \left(\mathbf{H}^T\mathbf{R}^{-1}\mathbf{H} + \mathbf{B}^{-1}\right)^{-1} = \mathbf{B} - \mathbf{B}\mathbf{H}^T\left(\mathbf{H}\mathbf{B}\mathbf{H}^T + \mathbf{R}\right)\mathbf{H}\mathbf{B} = \left(\nabla^2 J\right)^{-1}$$

The diagonal of **A** contains the posterior variances associated to H_2 fluxes, i.e., the square of the residual uncertainties on H_2 fluxes. The off-diagonal elements of **A** are the covariances $\mathbf{A}_{i,j}$, associated to H_2 fluxes that can be used to calculate the error correlations $\mathbf{C}_{i,j}$ for the different fluxes and regions according to

$$\mathbf{C}_{i,j} = \frac{\mathbf{A}_{i,j}}{\sqrt{\mathbf{A}_{i,i}\mathbf{A}_{j,j}}}$$

The typical size of the problem for a 14-year inversion is 30,000 observation constraints and 20,000 unknown fluxes. Solving this inverse problem by explicitly calculating $\mathbf{x}^a$ and **A** requires less than 1 h of calculation to run on a NEC-SX9 supercomputer.

2.6. Additional Constraint

[15] One additional constraint is incorporated into the inversion as a simple noise filter (see *Peylin et al.* [2002] for more details). In order to filter out possible unrealistic flux changes from one month to the next, these changes are kept limited to ±250% of the month-to-month difference of the prior fluxes. This limitation is tightened to ±30% for anthropogenic fluxes, which do not present a strong seasonal cycle. This filter links the fluxes in the time space. The impact of this additional constraint is studied in section 4. It makes additional lines in the jacobian matrix **H** and data in the y^0 vector and the **R** matrix. The ensemble of settings described above defines scenario S_0.

2.7. Fit to Observations

[16] After inversion, the fit to observed mixing ratios is largely improved as required by the minimization of the cost function. The north-to-south gradient is much better represented than the prior unbalanced budget (Figure 2). One should notice that the large-region approach of this study does not allow a perfect fit to observations as for inversions performed at model resolution which have much more degrees of freedom.

3. Scenarios and Sensitivity Inversions

3.1. Scenarios: Bringing Additional Information to Better Partition H_2 Sources and Sinks

[17] In this section, starting from the above scenario S_0, and using the diagnostic of error correlations for the optimized fluxes calculated by the inversion, we progressively build a more constrained prior scenario for H_2 sources and sinks (S_{ref}), using additional and independent information, with five intermediate scenarios in terms of constraints (S_1 to S_5).

[18] The ability of the inversion to infer separately the different regional sources and sinks of H_2 can be estimated semiquantitatively using the error correlations on the optimized fluxes (calculated from off diagonal terms of the **A** matrix, see section 2). It is only semiquantitative because assessing the level of significance of such a correlation coefficient is not trivial as we do not have directly access to the number of degrees of freedom of the system. However, error correlations getting close to −1 mean that the errors of two related fluxes are negatively correlated. Assuming a proportional link between the flux and its error implies that the two related fluxes tend to vary in opposite directions; when one increases the other decreases. Therefore two fluxes characterized by an error correlation close to −1 cannot be separated by the inversion and only a linear combination of these fluxes is properly constrained by the atmosphere. We have calculated the mean annual error correlations between the seven types of sources and sinks considered in this work: fossil fuel related emissions, N_2 fixation by ocean organisms, N_2 fixation by land organisms, photochemical production, biomass burning related emissions, soil uptake, and OH loss. Depending on the error correlations obtained, we have modified the original S_0 scenario, thus creating seven scenarios, culminating in the reference scenario S_{ref} (Table 1).

Table 1. Description of the Setup of the Seven Scenarios

	S_0	S_1	S_2	S_3	S_4	S_5	S_{ref}
OH loss uncertainty	±100%	±10%	±10%	±10%	±10%	±10%	±10%
Biomass burning IAV	no	no	yes	yes	yes	yes	yes
Biomass burning prior uncertainty	±100%	±100%	±10%	±10%	±10%	±10%	±10%
HCHO prior	LMDZ INCA	LMDZ INCA	LMDZ INCA	LMDZ INCA scaled by OMI	LMDZ INCA scaled by OMI	LMDZ INCA scaled by OMI	LMDZ INCA scaled by OMI
HCHO prior uncertainty	±7 Tg y^{-1}	±7 Tg y^{-1}	±7 Tg y^{-1}	±7 Tg y^{-1}	±5.8 Tg y^{-1} (85%)	±2.3 Tg y^{-1} (33%)	±1.2 Tg y^{-1} (15%)

[19] In scenario S_0, we assign a ±100% uncertainty on all prior monthly sources and sinks. This setting gives a large degree of freedom to the inversion to correct fluxes in order to fit H_2 observations. Prior fluxes in S_0 exhibit no interannual variations. Scenario S_0 presents a large negative error correlation (Figure 4) for OH loss versus total emissions ($r = -0.9$).

[20] We then define scenario S_1 in which the prior uncertainties for monthly OH loss are divided by a factor of 10, thus forcing OH loss to remain close to its prior interannually varying values. The impact of S_1 is to change the OH loss versus total emissions error correlation to −0.2 and the error correlation of soil uptake versus photochemical production from −0.7 to −0.8.

[21] In scenario S_2, the interannual prior values of biomass burning emissions are prescribed with uncertainties of ±10% (instead of constant prior values over years with ±100% uncertainties) from the GFED-V2 database of emissions [*van der Werf et al.*, 2006]. Prior uncertainties on all other sources are kept as in S_1. The biomass burning inventory has been available since 1997. Therefore in order to estimate year-to-year variations of biomass burning between 1991 and 1997, CO atmospheric observations from the NOAA/ESRL flask network are used to scale the H_2 biomass burning variability (CO observations are available since 1989). Doing so, one assumes that all the interannual variations of CO are due to biomass burning changes. Briefly, global mean CO time series and global H_2 emissions from GFED-V2 for 1997–2004 are used to determine the scaling factor which is then applied between 1991 and 1997 to global CO time series in order to estimate H_2 emissions from biomass burning. S_2 changes the initial value of the error correlation of biomass burning versus soil uptake from −0.3 to −0.16 but also degrades the error correlation of soil uptake versus photochemical production (−0.8 to −0.9) and of N_2 land fixation versus N_2 ocean fixation (−0.65 to −0.7). Constraining biomass burning limits the indeterminacy with biomass burning but transfers it to other fluxes. In S_2, the error correlations of the two largest fluxes in the H_2 budget are highly negatively cor-

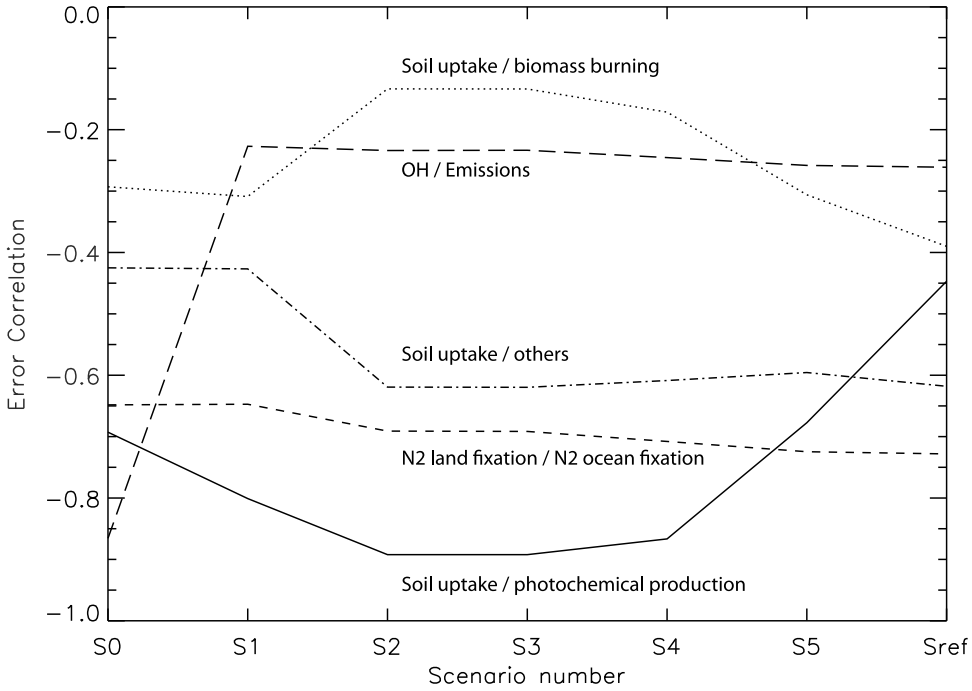

Figure 4. Error correlations r of several processes for the seven scenarios, calculated from the a posteriori covariance matrix A, for the long-term mean flux of each process over the 1991–2004 period.

related (−0.9), preventing them from being determined separately.

[22] In scenarios S_3, S_4, S_5, and S_{ref}, we try to address this issue by adding a constraint on the photochemical production of H_2 (biomass burning and OH loss are treated as in S_2). Almost all of the atmospheric production of H_2 occurs through formaldehyde oxidation [*Warneck*, 1988; Novelli *et al.*, 1999] We have compared the prior atmospheric columns of formaldehyde calculated by the LMDZ-INCA model (our prior estimate) with columns of formaldehyde retrieved with the Ozone Monitoring Instrument (OMI) on the EOS-Aura satellite since 2004 [*Levelt et al.*, 2006]. The OMI instrument is a nadir viewing imaging spectrograph that measures the solar radiation backscattered by the Earth's atmosphere and surface over the entire wavelength range from 270 to 500 nm with a spectral resolution of about 0.5 nm. It provides total columns of different gases such as ozone and formaldehyde. The average ratio of the modeled columns of HCHO divided by the satellite observed columns of HCHO are first calculated for each of the 12 regions defined in this work. The calculation of HCHO model columns is performed as a mean, weighted by the thickness of model pressure layers, which gives more weight to middle and high troposphere (300–700 hPa). The mean calculated ratio is applied as a correction to the prior estimate of the photochemical production of H_2 from LMDZ-INCA, assuming that 100% of the production comes from formaldehyde oxidation. Regional observed to modeled ratios range from 0.3 over South America to 2.0 over Boreal Eurasia.

[23] In scenario S_3, we apply the corrected photochemical production fluxes as a prior in each regional air column, keeping prior uncertainties as loose as in S_0. In scenarios S_4, S_5, and S_{ref}, the prior uncertainties on the monthly regional photochemical production, still corrected to match the satellite column data from OMI, are divided by a factor 20, 50, and 100, respectively. The annual prior uncertainty of the global photochemical production flux term is therefore reduced to 85% (S_4), 33% (S_5), and 15% (S_{ref}), respectively, of the prior uncertainty in the inversion S_3 (±7 Tg y^{-1}). Doing so, the OMI correction is gradually imposed to the prior photochemical production of H_2.

[24] Moving from S_3 to S_{ref}, the effect on error correlation of soil uptake versus photochemical production is important ($r = -0.70$ for S_4 and $r = -0.42$ only for S_{ref}). S_{ref} appears to largely limit the indeterminacy between the two main fluxes of the H_2 budget, just slightly degrading the other error correlations (Figure 4). This means that S_{ref} allows to better separate the main sources and sinks of H_2 than other scenarios developed here (S_0 to S_5). Therefore S_{ref} is now considered as our reference scenario.

[25] For other fluxes, the largest error correlations are found for fossil fuel related emissions with N_2 fixation related emissions from soils ($r = -0.4$) and with oceans ($r = -0.3$). The three emission fluxes, fossil and N_2 related emissions by lands and oceans, will be summed up in the following analysis as "others." Overall, we now consider the analysis of the optimized fluxes of H_2 for scenario S_{ref} and for five processes: photochemical production, soil uptake, biomass burning, OH loss, and others.

[26] The prior discretization of emissions into processes and regions allows us to calculate both process-based and region-based budgets. On a region-based point of view, error correlations between the different emissions over an inverted region for scenario S_{ref} range from −0.2 to −0.6. The largest negative-correlation stands for tropical South America versus tropical Asia (−0.6) and for Europe versus Asia (−0.4). Within a region, negative error correlation can also be found between processes (e.g., fossil related emissions in Europe versus soil uptake in Europe, $r = -0.6$), Between regions, for instance, errors for North Asia are found negatively correlated with errors for Europe ($r = -0.4$) and for North America ($r = -0.3$). On average, error correlations for total fluxes of a region are however smaller than for the global processes, indicating a better ability of the network to estimate the total fluxes by region than each process separately, even at larger spatial scales. In the following, accounting for the largest error correlations between the regions considered in the inversion, we have decided to discuss the fluxes for three groups of regions: northern regions (Europe, north Asia, North America), tropical regions (Africa, tropical South America, and tropical Asia) and southern regions (temperate South America and Oceania). The emerging results for individual regions within these three groups are also given in the text when relevant.

3.2. Sensitivity Inversions: Defining an External Uncertainty

[27] The residual uncertainty calculated by the inverse procedure (from **A** matrix, see section 2) does not represent the full uncertainty in the H_2 budget. We have therefore defined a range of uncertainty around scenario S_{ref} by running additional inversions to test the sensitivity of the modeled budget. To do so, we derive from the S_{ref} inversion 14 additional sensitivity inversions: (1) prior soil uptake divided by 2, (2) prior soil uptake multiplied by 2, (3) prior uncertainties on all fluxes divided by 2, (4) prior uncertainties on all fluxes multiplied by 2, (5) initial uncertainties on observations divided by 2, (6) initial uncertainties on observations multiplied by 2, (7) network of 56 NOAA sites only, (8) network of 18 sites present from 1991 to 2004, (9) network of 64 NOAA and CSIRO sites only, (10) network of 39 marine-influenced sites only, (11) no use of the noise filter (section 2), (12) constant offset between NOAA and CSIRO data (section 2), (13) variable offset between NOAA and CSIRO data (section 2), (14) prescribed OH fields without interannual variations.

[28] The standard deviation of the results of the 14 sensitivity inversions, of S_{ref} and of the six scenarios (S_0 to S_5), defines an "external" uncertainty on the H_2 budget, which complements the residual (Bayesian) uncertainty returned by the S_{ref} inversion. We assume the external uncertainty to be a proxy for all uncertainties not accounted for in the S_{ref} inversion setup (Table 3). Although probably underestimated, this complementary uncertainty makes the uncertainty of H_2 budget more realistic. The ensemble of 21 inversions is now used to study the H_2 budget (section 4) and its variability (section 5).

4. Global H_2 Budget

4.1. Overview of the H_2 Budget for the Seven Scenarios

[29] As expected from their characteristics, the main difference between the H_2 budgets of the seven scenarios presented above is the change in optimized H_2 soil uptake

Table 2. H_2 Budget for the 1991–2004 Period for the Seven Scenarios[a]

1991–2004	Prior (Range)	S_0	S_1	S_2	S_3	S_4	S_5	S_{ref}
Photochemical production	49 ± 2 (30–77)	36 ± 5	36 ± 5	36 ± 5	37 ± 5	38 ± 4	45 ± 2	48 ± 1
Soil uptake	−66 ± 13 (55–88)	−55 ± 4	−54 ± 4	−55 ± 4	−54 ± 4	−55 ± 4	−60 ± 3	−62 ± 3
Biomass burning and biofuel	10 ± 5 (10–20)	11 ± 4	11 ± 4	11 ± 2	10 ± 2	10 ± 2	10 ± 2	10 ± 1
Others	28 ± 7 (20–31)	26 ± 3	26 ± 3	26 ± 3	24 ± 3	25 ± 3	23 ± 3	22 ± 3
OH loss	−18 ± 3 (15–19)	−18 ± 3	−17 ± 1	−18 ± 1	−17 ± 1	−18 ± 1	−18 ± 1	−18 ± 1

[a]Measured in Tg y^{-1}. Processes are split into five categories: photochemical production, biomass burning, soil uptake, others (fossil fuels and N_2 fixation related emissions), and OH loss. Mean optimized annual fluxes over the 1991–2004 period are given with the residual uncertainty returned by the inversion. Magnitudes of prior fluxes and uncertainties for scenario S_0 are given together with the range found in the synthesis of *Ehhalt and Rohrer* [2009] (second column).

(Table 2). The value of this flux ranges from −54 Tg y^{-1} in S_0 to −62 Tg y^{-1} in S_{ref}, mostly depending upon the constraint imposed on the prior photochemical production, from 36 Tg y^{-1} in S_0 to 48 Tg y^{-1} in S_{ref}, in which this flux is provided by the OMI formaldehyde satellite data. Other emissions (biomass burning, fossil, and N_2 related emissions) are very close among the seven scenarios (~10 Tg y^{-1} for biomass burning and 22–26 Tg y^{-1} for fossil and N_2 related emissions).

4.2. Detailed H_2 Budget for S_{ref}

[30] Optimized fluxes and uncertainties for S_{ref}, for the three groups of regions, and for the five categories are given in Table 3. The first uncertainty attached to each flux is the residual uncertainty, returned by the inverse calculation as in Table 2. The second uncertainty is the external uncertainty, calculated from the sensitivity inversions (see section 3.2).

[31] On a process-based view (Table 3), our estimate of photochemical production for S_{ref} (48 ± 1 ± 4 Tg y^{-1}) is in the range of published studies summarized by *Ehhalt and Rohrer* [2009] (30–77 Tg y^{-1}). Photochemical production is the dominant flux in the tropics (+18 Tg y^{-1}). Fossil fuel and N_2 fixation emissions of H_2 over lands and oceans represent an additional flux of 22 ± 3 ± 3 Tg y^{-1} (+15 Tg y^{-1} in the NH regions), in the lower range of published results (20 to 31 Tg y^{-1}). The biomass burning emissions are 10 ± 1 ± 2 Tg y^{-1} over 1991–2004, mostly in the tropics (+8 Tg y^{-1}). This is in the lower range of published studies, 10–20 Tg y^{-1} as summarized in Table 1. The sum of all the sources of H_2 is 80 ± 4 ± 7 Tg y^{-1} (70 to 107 Tg y^{-1} for published studies), with a partition of 32/32/15 Tg y^{-1} for NH/tropical/SH regions, respectively. The OH sink alone represents a loss of ~18 Tg y^{-1} of H_2 (50% in the tropical regions), in the medium range of previous studies (15–19 Tg y^{-1}). Residual uncertainties on the OH sink are meaningless here because OH concentration is prescribed with a small prior uncertainty in scenario S_{ref}. Finally, given a rather small biomass burning emission and a medium to high OH sink, our estimate of the soil uptake of H_2 is −62 ± 3 ± 3 Tg y^{-1} (~50% in the NH regions), lying in the lower range of published results (−55 to −88 Tg y^{-1}).

[32] In our study, the H_2 soil uptake represents 77% of the total sink, whereas the OH sink represents the remaining 23%. H_2 tropospheric lifetime is estimated to be 2.0 ± 0.3 years for scenario S_{ref}, with a value of 2.7 ± 0.4 years for soil uptake and 8.6 ± 0.6 years for OH loss (1-sigma). Interestingly, one can notice that the photochemical production inferred in this inversion is compatible with most bottom-up estimates as summarized by *Ehhalt and Rohrer* [2009]; it is lower than previously published inversions and therefore does not require a corresponding large soil uptake to close the H_2 budget as in the work of *Xiao et al.* [2007]. This result is essentially due to our choice of constraining photochemical production with OMI satellite data.

4.3. Impacts of Additional Constraint and of Sensitivity Tests

[33] The noise filter in the flux space imposed as an additional constraint (section 2) has only a small impact on the annual fluxes. If no constraint is applied to limit the month-to-month flux changes, more noisy monthly fluxes are found, but the annual fluxes are not significantly modified for the three regions and the global processes.

[34] The different sensitivity tests performed allow defining an external uncertainty (section 3.2). The two tests producing the largest changes in terms of interannual variations are the ones with reduced prior uncertainties on observations and increased uncertainties on prior fluxes. Both tests generate more variable fluxes either because a

Table 3. Optimized H_2 Budget for the Period 1991–2004 Based on Scenario S_{ref} and All the Performed Sensitivity Tests[a]

1991–2004	NH Regions	Tropical Regions	SH Regions	Global
Photochemical production	16 ± 1 ± 4	18 ± 1 ± 4	14 ± 1 ± 4	**48 ± 1 ± 4**
Soil uptake	−32 ± 4 ± 4	−9 ± 4 ± 2	−20 ± 3 ± 1	**−62 ± 3 ± 3**
Biomass burning	1 ± 1 ± 1	8 ± 2 ± 3	<1	**10 ± 1 ± 2**
Others	15 ± 2 ± 2	6 ± 2 ± 1	<1	**22 ± 3 ± 3**
OH	−4 ± 1	−9 ± 1	−5 ± 1	**−18 ± 1**
Total	**−4 ± 1 ± 2**	**15 ± 2 ± 2**	**−11 ± 2 ± 2**	

[a]Measured in Tg y^{-1}. The fluxes and their uncertainties are given for five categories and for three groups of regions (see text). Global fluxes and total fluxes are also given (boldface entries). The first uncertainty is returned by the inversion (residual uncertainty). The second uncertainty is the standard deviation of the all the sensitivity inversions. Totals or global budget may not be balanced because of rounding errors. Uncertainties on OH loss are small because these fluxes are prescribed with small prior uncertainties in S_{ref} and most sensitivity tests (see text).

better fit to observations is required or because prior fluxes can vary more than in the S_{ref} inversion.

[35] Among the different sensitivity tests performed, the ones concerning network offsets are of particular importance for H_2 because no international measurement scale exists such as for carbon dioxide or methane. We first performed two sensitivity tests. In the first test, the CSIRO data are converted to the NOAA scale according to the two-line fit described in section 2 (changes from −19 ppb to −3 ppb). In the second test, the CSIRO data are converted by adding a constant offset of 10 ppb (equal to the mean of the variable offset of the first test), in order to calculate the impact of an error of the slopes of the fitted lines, on the estimated fluxes These two tests do not produce major changes in the inferred regional fluxes. Yearly global emissions are increased by up to 3 Tg y^{-1}, mainly south of 30°N, whereas global sinks are reduced by the same amount. The most impacted region is Oceania (+2 Tg y^{-1} on average), being influenced by the five CSIRO stations influencing the inverted fluxes for this region (CGO, MQA, MAA, CFA, and SPO). Largest flux changes are found in the early 1990s, consistent with the larger offsets applied for this period (variable offset test). The flux changes are found in tropical regions and Europe and only lead to small to negligible changes in the flux long-term trends.

[36] Applying an offset can be done in two directions: increasing CSIRO observations (as we did above) or decreasing NOAA observations. As this choice is arbitrary, we also performed the opposed tests and decreased NOAA observations by the same two offsets (constant and variable). Surprisingly, the changes in the regional H_2 flux anomalies go in the same direction as when CSIRO observations are increased. As the number of NOAA sites included in the inversion is much larger than the number of CSIRO sites (up to 54 versus up to 8), and because NOAA sites cover all regions with observations, the impact of decreasing NOAA observations is global: the global offset C_0 inferred by the inversion to represent the initial conditions in 1991 is reduced by 11 ppb in the case of a constant offset, and by 19 ppb in the case of a variable offset when applying corrections to NOAA stations instead of CSIRO stations.

5. Variability of the H_2 Sources and Sinks

[37] The ensemble of all performed inversions (scenario S_{ref}, 14 sensitivity inversions around S_{ref}, and scenarios S_0 to S_5) is used to study the seasonal, year-to-year, and trend variations of H_2 sources and sinks. This makes an ensemble of 21 inversions to study H_2 variability.

5.1. Seasonal Variations

[38] The mean seasonal cycle of H_2 sources and sinks over the period 1991–2004 has been calculated using the ensemble of all performed inversions (gray areas on Figure 5). The seasonal variations of scenarios S_{ref} (solid line) and S_0 (dashed line) are plotted on the top of this range as two extreme cases, together with prior fluxes (dotted line). The H_2 sources and sinks for the five groups of processes (fires emission, OH sink, soil sink, fossil fuel and N-fixation related emission, HCHO production) and the three groups of regions (NH, tropics, SH) previously defined are shown in Figure 5. The sum of the regional fluxes gives the global fluxes for each process (last plot on the right of each line). The total flux for each group of regions is shown at the bottom of each column.

[39] The H_2 sources and sinks showing the largest seasonal variations are the photochemical production and the soil uptake in northern regions, biomass burning in the tropics, and OH loss in the extratopics (Figure 5).

[40] In the northern regions, the photochemical production has a peak-to-peak amplitude of ~30 Tg y^{-1}. This source has a maximum in July and a minimum in winter. It varies in phase with the OH sink (maximum in July and minimum in winter) and in phase with the soil uptake (peak-to-peak amplitude of ~20 Tg y^{-1}, maximum in July–August, and minimum in winter). The different inversions performed tend to reduce the peak-to-peak amplitude of the seasonal cycle of both photochemical production and soil uptake in the northern regions as compared to the prior estimate. However, the peak-to-peak amplitude of S_{ref} is very close to the prior estimate for photochemical production, contrary to the one of S_0 (dashed line on Figure 5). Being in phase, the relative magnitudes of these two fluxes are only weakly constrained because they have opposite signs; a similar contribution at the sparse surface measurement stations can be produced by increasing or decreasing these two fluxes simultaneously. The fossil fuel and N_2-fixation related emissions show a seasonal cycle with emissions related to N_2 fixation being ~4 Tg y^{-1} larger during the growing season (May–August) compared to the other months (Figure 5, left). Overall the peak-to-peak seasonal cycle of the total emissions for the three northern regions (North America, north Asia, and Europe) ranges from 5 to 10 Tg y^{-1}, being the largest in north Asia (not shown).

[41] In the tropical regions, seasonal variations are mostly due to biomass burning which shows a double peak annual cycle (March and August–September) with a peak-to-peak amplitude of ~7 Tg y^{-1} for the March peak and ~10 Tg y^{-1} for the August–September peak. The March peak is associated with biomass burning in the northern tropics and the August–September peak is due to biomass burning in the southern tropics, consistent with the dry seasons of both hemispheres. This double peak structure is visible in the three tropical regions (South America, Africa, and tropical Asia, not shown). Soil uptake in the tropics shows a small seasonal cycle, although larger than for prior estimate, with a maximum in May and a minimum in November.

[42] In southern regions, the seasonal variations are smaller than for northern regions, except for the photochemical production, which has a peak-to-peak amplitude of ~15 Tg y^{-1}, and for OH loss (~5 Tg y^{-1}). Among the different sensitivity inversions, the southern surface emissions are reduced from the prior estimates and the soil uptake is slightly increased, producing a ~5 Tg y^{-1} decrease for the surface annual mean, which offsets the increase in the tropical regions, as compared to the prior estimate. These changes are related to the necessity to match the atmospheric surface north-to-south gradient of H_2 in the inversion (Figure 2).

[43] At the global scale, as photochemical production is seasonally compensated by OH loss and H_2 deposition, the seasonal variations of the global total H_2 flux are dominated by the seasonality of biomass burning in the tropics (Figure 5, bottom right).

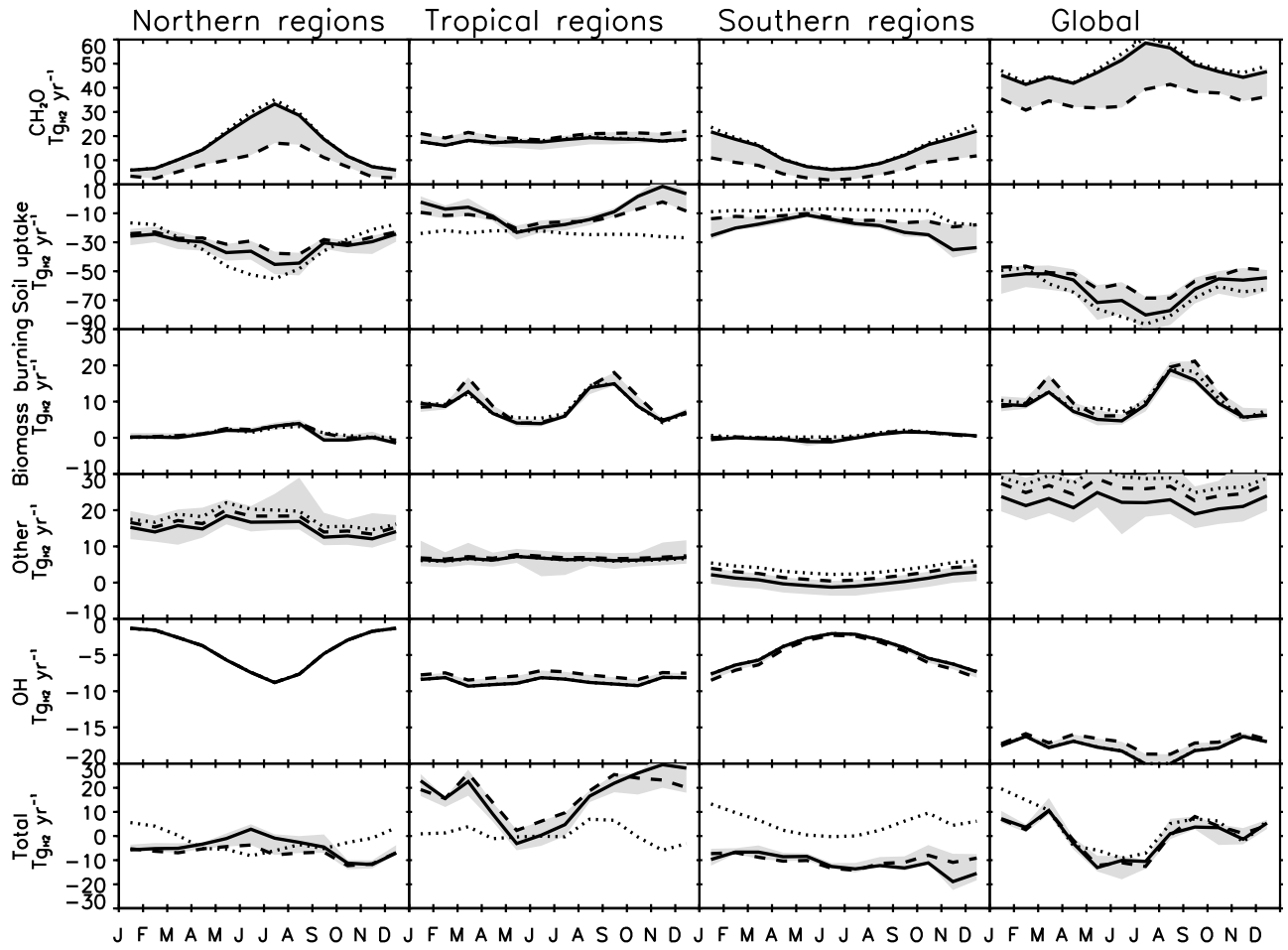

Figure 5. Mean Seasonal variations of H_2 sources and sinks, as inferred by the inversion, in Tg y^{-1} for the 1991–2004 period. H_2 fluxes for photochemical production (top), soil uptake, biomass and biofuel burning emissions, other emissions (fossil fuel and N_2 related emissions), OH loss, and total flux (bottom) are plotted for three groups of regions (first three columns on the left), and globally (last column on the right). The three regions are northern regions (North America, Europe, north Asia, North Atlantic, North Pacific), tropical regions (tropical America, Africa, tropical Asia, tropical oceans) and southern regions (South America temperate, Oceania). The region partition is based on TRANSCOM map (see text). Solid line represents the results of S_{ref}, dotted line is the prior and dashed line stands for S_0 (see Table 1). The gray area represents the range of the ensemble of inversions performed. The scale is not always the same for all plots.

5.2. Year-to-Year Variability

[44] The interannual variability of the global H_2 source is dominated by a large positive anomaly of 9 ± 2 Tg explained by higher biomass burning during the 1997–98 El Niño, mostly over the tropical regions (Figure 6). Accounting for this anomaly produces an overall interannual variability of ±3 Tg y^{-1} (1 sigma) for global H_2 fluxes. This variability drops to ±1 Tg y^{-1} only when omitting the 1997–1998 anomaly. Soil uptake also presents significant interannual variations. Increased tropical soil uptake is found in 1997–1998, whereas 1991–1992 and 2001–2002 are two periods with reduced soil uptake in the tropics. Northern regions show a trend in soil uptake that is analyzed in section 6. Photochemical production, as constrained by OMI, only shows little variation because of rather small interannual variations inferred from the OMI retrievals (see section 3.1).

[45] The 1997–1998 anomaly is not inferred from the atmospheric observations but results from the prior emissions from [*van der Werf et al.*, 2006]. Most of this anomaly is located in tropical Asia (not shown). Indeed, if the inversion is prescribed with a climatological prior like in S_0 (no interannual variations), the 1997–1998 anomaly is not attributed to biomass burning (dashed line on Figure 6 for tropical regions). In other words, when using prior interannually flat prior emissions for biomass burning in scenarios S_0 and S_1, the atmospheric network is unable to retrieve an anomalous biomass burning flux and the large atmospheric growth rate anomaly is spread among all sources and sinks (photochemical production, soil uptake, and biomass burning). This result means that the differences

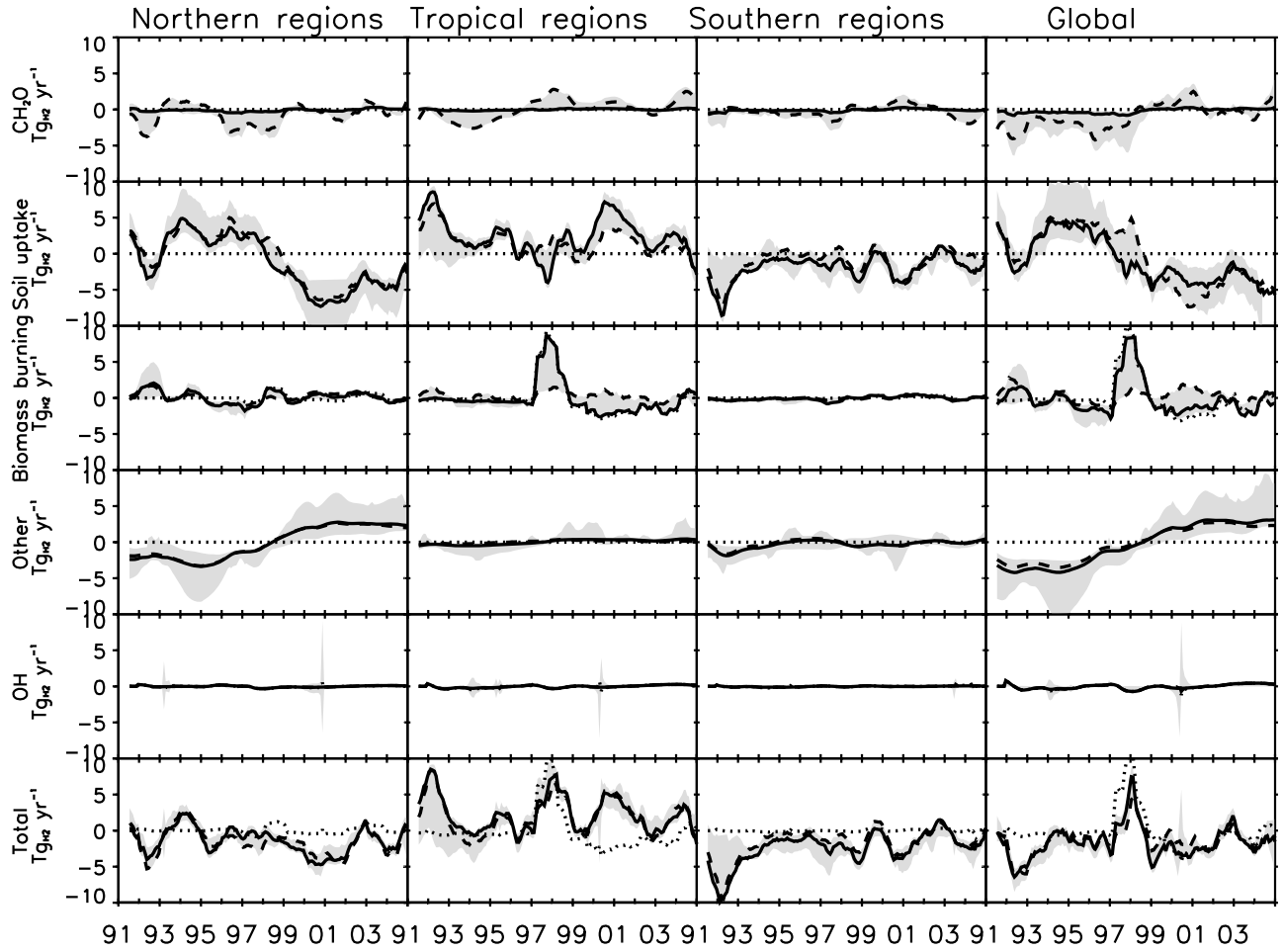

Figure 6. Interannual variations of H_2 sources and sinks, as inferred by the inversion, in Tg y^{-1} for the 1991–2004 period. Deseasonalized H_2 fluxes for photochemical production (top), soil uptake, biomass and biofuel burning emissions, other emissions (fossil fuel and N_2 related emissions), OH loss, and total flux (bottom) are plotted for three groups of regions (first three columns on the left), and globally (last column on the right). The three regions are northern regions (North America, Europe, north Asia, North Atlantic, North Pacific), tropical regions (tropical America, Africa, tropical Asia, tropical oceans) and southern regions (South America temperate, Oceania). The region partition is based on TRANSCOM map (see text). A 12-month running mean is applied to the inverted monthly fluxes to calculate the deseasonalized values. Solid line represents the results of S_{ref}, dotted line is the prior and dashed line stands for S_0 (see Table 1). The gray area represents the range of the ensemble inversions performed. The scale is always the same for all plots.

in the spatiotemporal distributions of H_2 sources and sinks are not sufficient to allow the (sparse) atmospheric network to distinguish photochemical production, biomass burning, soil uptake, fossil fuels, and N_2 fixation related emissions.

6. Long-Term Trend and Mean of the Soil Uptake

[46] Soil uptake represents the largest flux of the H_2 budget. In this section, the robustness of the long-term trend and of the long-term mean of H_2 soil uptake are discussed.

6.1. Long-Term Trend of the Soil Uptake

[47] One intriguing result of this study is the negative trend inferred for the global soil uptake (-0.7 ± 0.3 Tg y^{-1}) between 1991 and 2004. This trend is mostly due to the northern regions, with only a small contribution of tropical regions (Figure 6). In order to find the underlying processes explaining such a trend, the inverted anomaly of H_2 global soil uptake was compared with the bottom-up global soil uptake calculated by the LPJ-Why-Me vegetation model for the same period [*Wania et al.*, 2010]. Following *Smith-Downey et al.* [2006] and *Yonemura et al.* [2000a, 2000b], H_2 uptake by soils is modeled using a diffusion-consumption approach modified by various masks inhibiting diffusion [*Foster et al.*, 2009]. The LPJ-Why-Me global estimate of H_2 soil uptake over the 1991–2004 period is -60 ± 4 TgH_2 y^{-1}, which agrees very well in magnitude with our estimate of $-62 \pm 3 \pm 3$ Tg y^{-1}. Global soil uptake modeled by LPJ-Why-Me gives a significant trend of -0.12 ± 0.04 Tg y^{-1} and a correlation of R = 0.55 with our inverted soil uptake anomaly. However, the LPJ-Why-Me

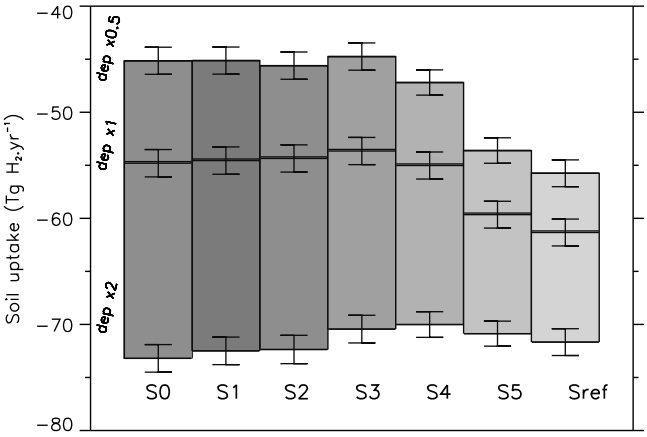

Figure 7. Bar plot of the H_2 soil uptake estimated with the seven inversion scenarios (see text). Each bar is defined by the three inversions performed for each scenario: bottom of the bar is the mean estimated soil uptake when the prior soil uptake is multiplied by 2 (dep x2), top of the bar is the mean estimated soil uptake when the prior soil uptake is divided by 2 (dep x0.5, and intermediate value is given by the control inversion of each scenario (dep x1). Uncertainties are the residual uncertainties given by the inversion for each inversion. The smaller the bar, the more robust is the estimate of the soil uptake.

soil uptake is 4 times less variable (1-sigma) and its trend is 6 times smaller in magnitude than in the inversion. This could mean a too weak response in the LPJ-Why-Me model to its drivers or a too strong variability inferred from the atmospheric inversion. The qualitative agreement in the sign of the trend is encouraging but large regional discrepancies remain between the top-down and the bottom-up approaches at this stage. Some previous studies concluded that soil moisture was the main driver of H_2 uptake by soils [*Schmitt et al.*, 2009; *Yonemura et al.*, 2000a, 2000b]. On the contrary, in LPJ-Why-Me, the main driver of H_2 soil uptake is the soil temperature (Pearson's correlation R~0.8), and not the soil moisture ($R < 0.2$). The long-term trend is therefore explained by an increase in the global soil temperature since the 1990s. More work is needed to better understand the underlying processes responsible for long-term variations of H_2 soil uptake.

[48] The H_2 budget per groups of regions does not present a significant trend over time (bottom line of Figure 6), which is consistent with the absence of a significant long-term trend in the atmospheric observations of H_2. Therefore another H_2 flux has to compensate (at least in the inversion) for the increasing trend of the soil uptake. The sum of fossil-fuel and N_2-fixation related emissions do present a positive trend of $+0.6 \pm 0.2$ Tg y^{-1}, especially after 1995, possibly reflecting increased economic growth in the middle 1990s to early 2000s (Figure 6). However, this increase is not reflected in the inventories of fossil fuel related CO emissions that do not exhibit an increase for these 2 decades (http://edgar.jrc.ec.europa.eu). Moreover, the error correlations r (after inversion) between the sum of fossil-fuel and N_2 related emissions and the soil uptake sink vary between $r = -0.4$ and $r = -0.6$ depending on the scenario. These values suggest that the two fluxes are not retrieved completely independently by the inversion. Indeed, the smallest absolute trend for both fluxes is found in the same inversion (S_{ref} + the smallest number of stations): −0.25 Tg y^{-1} for soil uptake and +0.15 Tg y^{-1} for fossil fuel and N_2 related emissions. Conversely, the largest absolute trend for both fluxes is also found in the same inversion (S_{ref} + observation error divided by 2): −1.3 Tg y^{-1} for soil uptake and +1.3 Tg y^{-1} for fossil fuel and N_2 related emissions. In this case, tighter observation error increases the constraint on H_2 sources and sinks and their variations are amplified to improve the fit to observations. As already noted (section 3.1), the error correlations between the total soil uptake and the total photochemical production may also contribute to the negative correlation in flux trends visible in Figure 6.

[49] Overall, it appears that the magnitude of the trend in soil uptake is not a robust result of the inversion, which makes it difficult to test the conclusions of the process-based LPJ-Why-Me ecosystem model. However, we note that both independent approaches produce a negative trend for H_2 global soil uptake between 1991 and 2004, compensated, in the inversions, by an increase in emissions (mostly fossil and N_2 related emissions).

6.2. Long-Term Mean of the Soil Uptake

[50] In order to evaluate the robustness of the soil uptake long-term mean (−62 Tg y^{-1}), we have complemented each of the seven scenarios (Table 1) by two additional inversions, starting with a soil uptake global magnitude that is half (−33 Tg y^{-1}) or twice (−132 Tg y^{-1}) of the magnitude assigned to the prior in the control inversion (−66 Tg y^{-1}) of each scenario. The absolute prior uncertainties are kept the same in the three inversions. The spread between the three inversions of each scenario is used as a measure of the robustness of the inverted H_2 soil uptake. Starting from the less constrained scenario (S_0) and moving toward the more constrained one (S_{ref}), the mean values of the soil uptake (1991–2004) and their residual uncertainties for the three inversions are shown in Figure 7. For S_0, the posterior value of global H_2 sink is statistically different (-73 ± 4 Tg y^{-1}, $p < 0.0001$ and -45 ± 2 Tg y^{-1}, $p < 0.0001$, respectively) from the standard inversion (-55 ± 3 Tg y^{-1}). A p-value smaller than 0.0001 indicates that there is less than 0.01% probability that the two values of the mean soil uptake are identical. This means that the estimate of the inverted H_2 soil uptake flux is not very robust for S_0. However, the optimized H_2 soil uptake flux in the two complementary inversions departs significantly from their prior estimate (−132 and −33 Tg y^{-1}, respectively) and converge toward an intermediate value. In S_0, neither the spatiotemporal distribution of prior sources and sinks nor the isotope-derived constraint on the global source provide a strong enough constraint to quantify separately the different H_2 sources and sinks, in particular the soil sink, even at the global scale.

[51] In scenario S_1 (tighter OH constraint) and S_2 (+ tighter biomass burning constraint) the range of the soil uptake estimates is almost unchanged as compared to S_0. For S_1, this can be understood because the OH sink only represents ~20% of the total H_2 sink and thus reducing the prior errors on that sink translates into a small impact on optimized H_2 fluxes. For S_2, biomass burning is a rather small flux (~10 Tg y^{-1}) and its variations imposed from GFED_V2 do not influence largely the mean soil uptake

(6 to 7 times larger in magnitude). However, as previously noted, prescribing the biomass burning flux significantly modifies the mix of source anomalies that are responsible for the 1997–1998 El Niño based signals.

[52] The impact on the optimized global H_2 soil uptake estimation of the gradual nudging of the photochemical production with OMI data (scenarios S_3, S_4, S_5, and S_{ref}) is important, with a significant increase of the long-term mean soil uptake from –54 Tg y^{-1} for S_3 to −62 Tg y^{-1} for S_{ref} (Figure 7). For S_{ref}, the global mean H_2 soil uptake still ranges from −56 ± 3 Tg y^{-1} ($p = 0.001$) to −72 ± 3 Tg y^{-1} ($p < 0.0001$). Although more consistent, the value of the long-term mean soil uptake cannot be considered as statistically consistent between the three inversions using different prior values of the soil uptake.

[53] In summary, a tight constraint on the photochemical production flux, here given by OMI formaldehyde data, improves the robustness of the mean H_2 soil uptake estimate, although not making it statistically robust. In addition, prescribing interannually varying biomass burning emissions does not greatly influence the mean soil uptake but constrains the partition of the year-to-year variations of major H_2 fluxes especially during the 1997–1998 El Niño.

7. Conclusions

[54] We present the results of an atmospheric inversion of H_2 sources and sinks for the period 1991–2004. This work gives a complete view of H_2 sources and sinks both in terms of budgets, in terms of variations (seasonal, interannual, and trends), and in terms of uncertainties. Overall, our results support prior work which has outlined the atmospheric H_2 budget (Table 2), i.e., 48 Tg y^{-1} for photochemical production, 10 Tg y^{-1} for biomass and biofuel burning, 22 Tg y^{-1} for fossil fuel and N_2 related emissions, −62 Tg y^{-1} for soil uptake, −18 Tg y^{-1} for OH loss. The lifetime of H_2 is found to be ~2 years, as in most previous studies [*Ehhalt and Rohrer*, 2009], with the noticeable exception of *Rhee et al.* [2006] who found 1.4 ± 0.2 y only because of a large global sink strength of 107 ± 11 Tg y^{-1}, compared to our value of −80 Tg y^{-1}.

[55] One important result of our study is that additional information is needed beyond H_2 observations in order to significantly improve the robustness of the inverted H_2 soil uptake and of interannual variations. In other words, H_2 observations from the flask network alone are insufficient to determine a robust process-based budget of H_2 sources and sinks at a regional scale. This result can appear surprising considering that various authors produced robust process based budgets for other gases such as methane [*Bergamaschi et al.*, 2005] or carbon monoxide [*Pétron et al.*, 2004]. The difficulty with H_2 may be the more diffuse characteristics of some H_2 fluxes. CO has a shorter lifetime and most of its emissions are linked to relatively well-determined areas such as megacities and fire spots. CH_4 has a variety of emission types, some of which have specific characteristics in space (gas leakages or rice paddies) and/or in time (e.g., biomass burning or wetland emissions). For H_2, more than half of the emissions come from the volume of the atmosphere (photochemical production) and therefore produce less signal at a surface station than a surface source. The main sink (soil uptake) is also more diffuse than anthropogenic emissions or biomass burning spots. Most atmospheric inversions use prior information to regularize the inverse problem. Generally, prior constraints are rather loose to guide but not to nudge the estimated fluxes. Here, we have decided to go a step further and to prescribe some of the prior information with tighter errors, because atmospheric measurements of H_2 and loose prior fluxes could hardly partition all the different H_2 sources and sinks. In order to be able to estimate robustly the H_2 soil uptake, we used, with tight prior errors, a satellite-based database [*van der Werf et al.*, 2006] of biomass burning emissions, satellite retrievals of formaldehyde from OMI [*Levelt et al.*, 2006] to scale photochemical production, and a previous methyl chloroform inversion to scale OH loss [*Bousquet et al.*, 2005]. Doing so, we produce an estimate of H_2 deposition flux of −62 ± 3 ± 3 Tg y^{-1} for the period 1991–2004, representing about 3/4 of the total H_2 sink. A negative trend has been found for H_2 soil uptake, qualitatively consistent with the LPJ bottom-up vegetation model, but its magnitude appears to be not robust to the inversion setup. Without these additional constraints on the prior fluxes, the robustness of inversion results for H_2 soil uptake and for the variability of H_2 sources and sinks is found to be weak.

[56] Future inversions of H_2 sources and sinks should gain robustness by including observations of the deuterium enrichment of H_2 (δD of H_2), as shown in the work of *Price et al.* [2007] and *Rhee et al.* [2006]. In the troposphere δD is about +130 ± 4% [*Gerst and Quay*, 2000]. The isotopic signatures for fossil fuel, biofuel, biomass burning, and ocean sources are all depleted in δD relative to the atmosphere, whereas photochemical production of H_2 has a large positive isotopic signature. On the sink side, OH loss fractionates more than soil uptake [*Price et al.*, 2007]. Assimilating δD observations together with H_2 observations could therefore bring new constraints on H_2 budget if the different isotopic signatures can be determined with a reasonable precision. Several groups have produced δD observations [*Gerst and Quay*, 2001; *Rahn et al.*, 2003; *Röckmann et al.*, 2003; *Rhee et al.*, 2006; *Price et al.*, 2007]. The δD observations from six sampling sites are available for the recent years (from 2007) and, as soon as H_2 observations after 2005 will be available at NOAA, such a combined inversion could be performed and could also integrate the 14 new continuous measurement sites operated in Europe (http://www.iau.uni-frankfurt.de/eurohydros/) within the EUROHYDROS European network.

[57] **Acknowledgments.** French Atomic agency (CEA) and Laboratoire des Sciences du Climat et de l'Environnement (LSCE) are to be thanked to have provided computing time to this work trough the GENCI project. Part of this work is funded by French CNRS and by EU projects HYMN and EUROHYDROS. We acknowledge Guido Van der Werf for providing H_2 emissions from fires, and the OMI science team to make the OMI retrievals available. We acknowledge the TRANSCOM community for the region map used in this work. We thank Philippe Peylin for his contribution to the codes used in this work to analyze the data. Peter Rayner is the recipient of an Australian Research Council Professorial Fellowship (DP1096309).

References

Baker, D. F., et al. (2006), TransCom3 inversion intercomparison: Impact of transport model errors on the interannual variability of regional CO2

fluxes, 1988–2003, *Global Biogeochem. Cycles*, *20*, GB1002, doi:10.1029/2004GB002439.
Bergamaschi, P., et al. (2005), Inverse modelling of national and European CH4 emissions using the atmospheric zoom model TM5, *Atmos. Chem. Phys.*, *5*, 2431–2460, doi:10.5194/acp-5-2431-2005.
Bergamaschi, P., et al. (2009), Inverse modeling of global and regional CH_4 emissions using SCIAMACHY satellite retrievals, *J. Geophys. Res.*, *114*, D22301, doi:10.1029/2009JD012287.
Bousquet, P., P. Peylin, P. Ciais, C. Le Quere, P. Friedlingstein, and P. P. Tans (2000), Regional changes in carbon dioxide fluxes of land and oceans since 1980, *Science*, *290*(5495), 1342–1346, doi:10.1126/science.290.5495.1342.
Bousquet, P., D. A. Hauglustaine, P. Peylin, C. Carouge, and P. Ciais (2005), Two decades of OH variability as inferred by an inversion of atmospheric transport and chemistry of methyl chloroform, *Atmos. Chem. Phys.*, *5*, 2635–2656, doi:10.5194/acp-5-2635-2005.
Bousquet, P., et al. (2006), Contribution of anthropogenic and natural sources to atmospheric methane variability, *Nature*, *443*(7110), 439–443, doi:10.1038/nature05132.
Brasseur, G. P., D. A. Hauglustaine, S. Walters, R. J. Rasch, J.-F. Müller, C. Granier, and X. X. Tie (1998), MOZART, a global chemical transport model for ozone and related chemical tracers 1. Model description, *J. Geophys. Res.*, *103*(D21), 28,265–28,289, doi:10.1029/98JD02397.
Chen, Y. H., and R. G. Prinn (2006), Estimation of atmospheric methane emissions between 1996 and 2001 using a three-dimensional global chemical transport model, *J. Geophys. Res.*, *111*, D10307, doi:10.1029/2005JD006058.
Chevallier, F., M. Fisher, P. Peylin, S. Serrar, P. Bousquet, F.-M. Bréon, A. Chédin, and P. Ciais (2005), Inferring CO_2 sources and sinks from satellite observations: Method and application to TOVS data, *J. Geophys. Res.*, *110*, D24309, doi:10.1029/2005JD006390.
Chevallier, F., A. Fortems, P. Bousquet, I. Pison, S. Szopa, M. Devaux, and D. A. Hauglustaine (2009), African CO emissions between years 2000 and 2006 as estimated from MOPITT observations, *Biogeosciences*, *6* (1), 103–111, doi:10.5194/bg-6-103-2009.
Conrad, R., and W. Seiler (1980), Contribution of hydrogen production by biological nitrogen fixation to the global hydrogen budget, *J. Geophys. Res.*, *85*(C10), 5493–5498, doi:10.1029/JC085iC10p05493.
Conrad, R., and W. Seiler (1981), Decomposition of atmospheric hydrogen by soil microorganisms and soil enzymes, *Soil Biol. Biochem.*, *13*(1), 43–49, doi:10.1016/0038-0717(81)90101-2.
Ehhalt, D. H., and F. Rohrer (2009), The tropospheric cycle of H2: A critical review, *Tellus Ser. B*, *61*(3), 500–535.
Fortems-Cheiney, A., F. Chevallier, I. Pison, P. Bousquet, C. Carouge, C. Clerbaux, P.-F. Coheur, M. George, D. Hurtmans, and S. Szopa (2009), On the capability of IASI measurements to inform about CO surface emissions, *Atmos. Chem. Phys.*, *9*, 8735–8743, doi:10.5194/acp-9-8735-2009.
Foster, P., C. Prentice, and R. Wania (2009), Evaluation of the models ability to simulate observed trace gas fluxes from observations in different regions (Deliverable D2.2), report, Univ. of Bristol, Bristol, UK. (Available at http://www.knmi.nl.)
Francey, R. J., et al. (1998), Atmospheric carbon dioxide and its stable isotope ratios, methane, carbon monoxide, nitrous oxide and hydrogen from Shetland Isles, *Atmos. Environ.*, *32*(19), 3331–3338, doi:10.1016/S1352-2310(97)00491-3.
Gerst, S., and P. Quay (2000), The deuterium content of atmospheric molecular hydrogen: Method and initial measurements, *J. Geophys. Res.*, *105*(D21), 26,433–26,445, doi:10.1029/2000JD900387.
Gerst, S., and P. Quay (2001), Deuterium component of the global molecular hydrogen cycle, *J. Geophys. Res.*, *106*(D5), 5021–5031, doi:10.1029/2000JD900593.
GLOBALVIEW-CH_4 (2005), Cooperative atmospheric data integration project: Methane, CD-ROM, NOAA, Boulder, Colo. (Also available on Internet via anonymous FTP to ftp.cmdl.noaa.gov, Path: Ccg/ch4/GLOBALVIEW.)
Gurney, K. R., et al. (2002), Towards robust regional estimates of CO2 sources and sinks using atmospheric transport models, *Nature*, *415* (6872), 626–630, doi:10.1038/415626a.
Hauglustaine, D. A., and D. H. Ehhalt (2002), A three-dimensional model of molecular hydrogen in the troposphere, *J. Geophys. Res.*, *107*(D17), 4330, doi:10.1029/2001JD001156.
Hauglustaine, D. A., F. Hourdin, L. Jourdain, M.-A. Filiberti, S. Walters, J.-F. Lamarque, and E. A. Holland (2004), Interactive chemistry in the Laboratoire de Météorologie Dynamique general circulation model: Description and background tropospheric chemistry evaluation, *J. Geophys. Res.*, *109*, D04314, doi:10.1029/2003JD003957.
Hough, A. M. (1991), Development of a two-dimensional global tropospheric model: Model chemistry, *J. Geophys. Res.*, *96*, 7325–7362, doi:10.1029/90JD01327.
Hourdin, F., and O. Talagrand (2006), Eulerian backtracking of atmospheric tracers. I: Adjoint derivation and parametrization of subgrid-scale transport, *Q. J. R. Meteorol. Soc.*, *132*(615), 567–583, doi:10.1256/qj.03.198.A.
Kaminski, T., P. J. Rayner, M. Heimann, and I. G. Enting (2001), On aggregation errors in atmospheric transport inversions, *J. Geophys. Res.*, *106*, 4703–4715.
Krol, M., and J. Lelieveld (2003), Can the variability in tropospheric OH be deduced from measurements of 1,1,1-trichloroethane (methyl chloroform)? *J. Geophys. Res.*, *108*(D3), 4125, doi:10.1029/2002JD002423.
Langenfelds, R. L., R. J. Francey, B. C. Pak, L. P. Steele, J. Lloyd, C. M. Trudinger, and C. E. Allison (2002), Interannual growth rate variations of atmospheric CO 2 and its delta 13 C, H 2, CH 4, and CO between 1992 and 1999 linked to biomass burning, *Global Biogeochem. Cycles*, *16*(3), 1048, doi:10.1029/2001GB001466.
Levelt, P. F., et al. (2006), Science objectives of the ozone monitoring instrument, *IEEE Trans. Geosci. Remote Sens.*, *44*(5), 1199–1208, doi:10.1109/TGRS.2006.872336.
Muller, J. F. (1992), Geographical distribution and seasonal variation of surface emissions and deposition velocities of atmospheric trace gases, *J. Geophys. Res.*, *97*, 3787–3804.
Müller, J.-F., and G. Brasseur (1995), IMAGES: A three-dimensional chemical transport model of the global troposphere, *J. Geophys. Res.*, *100*(D8), 16,445–16,490, doi:10.1029/94JD03254.
Novelli, P. C., P. M. Lang, K. A. Masarie, D. F. Hurst, R. Myers, and J. W. Elkins (1999), Molecular hydrogen in the troposphere- Global distribution and budget, *J. Geophys. Res.*, *104*(D23), 30,427–30,444, doi:10.1029/1999JD900788.
Olivier, J. G. J., and J. J. M. Berdowski (2001), Global emissions sources and sinks, in *The Climate System*, edited by J. Berdowski, R. Guichert, and B. Heij, pp. 33–78, A. A. Balkema, Lisse, Netherlands.
Pétron, G., C. Granier, B. Khattatov, V. Yudin, J.-F. Lamarque, L. Emmons, J. Gille, and D. P. Edwards (2004), Monthly CO surface sources inventory based on the 2000–2001 MOPITT satellite data, *Geophys. Res. Lett.*, *31*, L21107, doi:10.1029/2004GL020560.
Peylin, P., D. Baker, J. Sarmiento, P. Ciais, and P. Bousquet (2002), Influence of transport uncertainty on annual mean and seasonal inversions of atmospheric CO_2 data, *J. Geophys. Res.*, *107*(D19), 4385, doi:10.1029/2001JD000857.
Pison, I., P. Bousquet, F. Chevallier, S. Szopa, and D. Hauglustaine (2009), Multi-species inversion of CH4, CO and H-2 emissions from surface measurements, *Atmos. Chem. Phys.*, *9*(14), 5281–5297, doi:10.5194/acp-9-5281-2009.
Price, H., L. Jaeglé, A. Rice, P. Quay, P. C. Novelli, and R. Gammon (2007), Global budget of molecular hydrogen and its deuterium content: Constraints from ground station, cruise, and aircraft observations, *J. Geophys. Res.*, *112*, D22108, doi:10.1029/2006JD008152.
Prinn, R. G., et al. (2005), Evidence for variability of atmospheric hydroxyl radicals over the past quarter century, *Geophys. Res. Lett.*, *32*, L07809, doi:10.1029/2004GL022228.
Rahn, T., J. M. Eiler, K. A. Boering, P. O. Wennberg, M. C. McCarthy, S. Tyler, S. Schauffler, S. Donnelly, and E. Atlas (2003), Extreme deuterium enrichment in stratospheric hydrogen and the global atmospheric budget of H2, *Nature*, *424*(6951), 918–921, doi:10.1038/nature01917.
Rayner, P., I. Enting, R. Francey, and R. Langenfeld (1999), Reconstructing the recent carbon cycle from atmospheric CO2, d13C and O2/N2 observations, *Tellus*, *51B*, 213–232.
Rhee, T. S., C. A. M. Brenninkmeijer, and T. Rockmann (2006), The overwhelming role of soils in the global atmospheric hydrogen cycle, *Atmos. Chem. Phys.*, *6*, 1611–1625, doi:10.5194/acp-6-1611-2006.
Röckmann, T., T. S. Rhee, and A. Engel (2003), Heavy hydrogen in the stratosphere, *Atmos. Chem. Phys.*, *3*, 2015–2023, doi:10.5194/acp-3-2015-2003.
Schmitt, S., A. Hanselman, U. Wollschalger, S. Hammer, and I. Levin (2009), Investigation of parameters controlling the soil sink of atmospheric molecular hydrogen, *Tellus*, *61B*, 416–423.
Schultz, M. G., T. Diehl, G. P. Brasseur, and W. Zittel (2003), Air pollution and climate forcing impacts of a global hydrogen economy, *Science*, *302*, 624–627, doi:10.1126/science.1089527.
Smith-Downey, N. V., J. T. Randerson, and J. M. Eiler (2006), Temperature and moisture dependence of soil H2 uptake measured in the laboratory, *Geophys. Res. Lett.*, *33*, L14813, doi:10.1029/2006GL026749.
Steele, L. P., E. J. Dlugokencky, P. M. Lang, P. P. Tans, R. C. Martin, and K. A. Masarie (1992), Slowing down of the global accumulation of atmospheric methane during the 1980's, *Nature*, *358*, 313–316, doi:10.1038/358313a0.
Tarantola, A. (1987), *Inverse Problem Theory*, Elsevier, Amsterdam.
Thoning, K. W., P. P. Tans, and W. D. Komhyr (1989), Atmospheric carbon dioxide at Mauna Loa Observatory. 2. Analysis of the NOAA

GMCC data, 1974, 1985, *J. Geophys. Res.*, *94*(D6), 8549–8565, doi:10.1029/JD094iD06p08549.

Uppala, S. M., et al. (2005), The ERA-40 reanalysis, *J. R. Meteorol. Soc.*, *131*, 2961–3012, doi:10.1256/qj.04.176.

van der Werf, G. R., J. T. Randerson, L. Giglio, G. J. Collatz, P. S. Kasibhatla, and A. F. Arellano (2006), Interannual variability in global biomass burning emissions from 1997 to 2004, *Atmos. Chem. Phys.*, *6*, 3423–3441, doi:10.5194/acp-6-3423-2006.

Wania, R., I. Ross, and I. C. Prentice (2010), Implementation and evaluation of a new methane model within a dynamic global vegetation model: LPJ-WHyMe v1.3, *Geosci. Model Dev. Discuss.*, *3*, 1–59, doi:10.5194/gmdd-3-1-2010.

Warneck, P. (1988), *Chemistry of the Natural Atmosphere*, *Int. Geophys. Ser.*, vol. 41, Academic, San Diego, Calif.

Warwick, N. J., S. Bekki, E. G. Nisbet, and J. A. Pyle (2004), Impact of a hydrogen economy on the stratosphere and troposphere studied in a 2-D model, *Geophys. Res. Lett.*, *31*, L05107, doi:10.1029/2003GL019224.

Xiao, X., et al. (2007), Optimal estimation of the soil uptake rate of molecular hydrogen from the Advanced Global Atmospheric Gases Experiment and other measurements, *J. Geophys. Res.*, *112*, D07303, doi:10.1029/2006JD007241.

Yonemura, S., S. Kawashima, and H. Tsuruta (1999), Continuous measurements of CO and H_2 deposition velocities onto an andisol: Uptake control by soil moisture, *Tellus Ser. B*, *51*, 688–700.

Yonemura, S., S. Kawashima, and H. Tsuruta (2000a), Carbon monoxide, hydrogen, and methane uptake by soils in a temperate arable field and a forest, *J. Geophys. Res.*, *105*, 14,347–14,362.

Yonemura, S., M. Yokozawa, S. Kawashima, and H. Tsuruta (2000b), Model analysis of the influence of gas diffusivity in soil on Co and H2 uptake, *Tellus Ser. B, 52*(3), 919–933.

Yver, C., M. Schmidt, P. Bousquet, W. Zahorowski, and M. Ramonet (2009), Estimation of the molecular hydrogen soil uptake and traffic emissions at a suburban site near Paris through hydrogen, carbon monoxide, and radon-222 semicontinuous measurements, *J. Geophys. Res.*, *114*, D18304, doi:10.1029/2009JD012122.

P. Bousquet, P. Ciais, A. Fortems, D. Hauglustaine, Y. S. Li, I. Pison, M. Ramonet, M. Schmidt, S. Szopa, and C. Yver, Laboratoire des Sciences du Climat et de l'Environnement, F-91191 Gif sur Yvette CEDEX, France. (philippe.bousquet@lsce.ipsl.fr)

P. Foster, Department of Earth Sciences, University of Bristol, BS8 1TH Bristol, UK.

R. Langenfelds and P. Steele, Centre for Australian Weather and Climate Research, CSIRO Marine and Atmospheric Research, Aspendale, VIC 3195, Australia.

C. Morfopoulos, Division of Biology, Imperial College of London, SW7 2AZ London, UK.

P. Novelli, Earth System Research Laboratory, NOAA, Boulder, CO 80305, USA.

P. J. Rayner, School of Earth Sciences, University of Melbourne, Parkville, Vic 3010, Australia.